Recursive Flow Matching

Jiahe Huang [1] **Sihan Xu** [2] **Sharvaree Vadgama** [1] **Rose Yu** [1]

Abstract

Generative models have emerged as a powerful paradigm for solving physics systems and modeling complex spatiotemporal dynamics. However, achieving high physical accuracy without incurring high computational cost remains a fundamental challenge, as existing approaches face a critical speed-fidelity trade-off. In this work, we introduce **Recursive Flow Matching** (*RecFM*), a generative framework for forecasting complex spatiotemporal dynamics. RecFM enforces self-consistency to align trajectories across discretization scales, reducing discretization errors and improving performance across metrics for physics-based tasks. To our knowledge, this is the first method to achieve high-fidelity one- and few-step (*2-4 step*) dynamic generation for scientific systems with performance comparable to state-of-the-art multi-step solvers. Across challenging scientific benchmarks, RecFM achieves up to a $20\times$ speedup over leading diffusion-based emulators while improving predictive accuracy. Furthermore, RecFM reduces mean squared error by over 15% compared to vanilla flow matching, offering a scalable and efficient solution for real-time scientific emulation. Project page: jh-huangchloe.github.io/RecFM/.

1. Introduction

Predicting the evolution of physical systems is a fundamental challenge in scientific computing, with applications ranging from fluid dynamics to climate modeling and weather forecasting. Traditional numerical solvers provide high-fidelity solutions (Dhatt et al., 2012; Cantwell et al., 2015), but are typically computationally expensive and impractical for real-time or large-scale deployment. These limitations motivate the need for data-driven approaches that can efficiently model complex, high-dimensional dynamics. With advancements in scientific machine learning approaches like neural operators (Kovachki et al., 2023; Li et al., 2020; Lu et al., 2021) and PINNs (Raissi et al., 2019; Penwarden et al., 2022) are widely used to simulate systems described by partial differential equations (PDEs). However, in real-world applications, these governing equations are frequently incomplete, computationally prohibitive, or challenging to formulate for complex and stochastic systems such as climate dynamics.

Recent advances in generative modeling provide a powerful framework for learning high-frequency data distributions tailored to scientific applications, addressing key challenges in molecular design (Abramson et al., 2024; Shen et al., 2025), material generation (Zeni et al., 2025), and climate modeling (Duncan et al., 2025; Watt-Meyer et al., 2025). In these fields, the ability of generative models to quantify uncertainty and manage sparse or irregular measurements offers significant advantages over traditional deterministic methods. Especially in computational physics, generative methods have been shown to reconstruct spatiotemporal dynamics from limited observations, such as turbulent fluid flow or atmospheric models, effectively bridging the gap between inductive statistical learning and deductive physical laws (Cachay et al., 2025; Huang et al., 2024; Rühling Cachay et al., 2023; Zhuang et al., 2025). Nevertheless, deploying these models for accurate dynamical prediction remains challenging, as they must balance efficiency with the preservation of physical fidelity over time.

A key limitation of diffusion-based models is their inherently iterative inference procedure, which requires tens to hundreds of sequential denoising steps to produce high-quality predictions (Ho et al., 2020; Karras et al., 2022; Song et al., 2020; Nichol & Dhariwal, 2021). This results in significant computational overhead, especially for time-dependent simulations. To address this issue, continuous normalizing flows (CNFs) (Mathieu & Nickel, 2020) and flow matching (FM) (Chen & Lipman, 2023; Geng et al., 2025; Lipman et al., 2022) have emerged as efficient alternatives, learning continuous vector fields that define probability paths without requiring simulation during training. While these approaches reduce the number of required function evaluations, a fundamental trade-off remains: reducing the number of inference steps often leads to degraded ac-

[1]University of California, San Diego [2]University of Michigan. Correspondence to: Jiahe Huang <chh118@ucsd.edu>, Rose Yu <roseyu@ucsd.edu>.

Accepted by the AI for Science workshop (ICML 2026), Seoul, South Korea. Copyright 2026 by the author(s).

(a) Flow Matching *(b)* Recursive Flow Matching

Figure 1. **Comparison of flow matching paradigms.** (a) Flow Matching (FM) learns a direct trajectory that transports samples from the data distribution (x_0) to the noise distribution (x_1). (b) Recursive Flow Matching (RecFM) augments this with recursively scaled trajectories (brown, blue, and red arrows) that intersect at shared spatial states (x_t), enabling cross-scale trajectory alignment and consistency training along the flow.

curacy and instability, particularly in long-term dynamical rollouts.

To further accelerate these systems, a wide range of approaches have been proposed, including consistency models and distillation-based methods (Tauberschmidt et al., 2025; Xu et al., 2023b). Consistency models, such as Shortcut Diffusion (Frans et al., 2024), introduce self-consistency constraints that enable direct mapping along the probabilistic path in a single step, while distillation techniques aim to compress multi-step generation into an efficient student model (Song et al., 2024). However, a key challenge in these approaches is preserving the spectral richness and spatiotemporal fidelity of physical fields, as aggressive step reduction often smooths out high-frequency structures that are critical for accurate scientific simulations (Xu et al., 2025). These limitations highlight the need for a framework that can achieve efficient few-step (typically *at most four steps*) generation while maintaining trajectory fidelity and stability.

To address these challenges, we introduce **Recursive Flow Matching** (*RecFM*), a generative framework for stable and efficient modeling of dynamical systems. Instead of relying on a single discretized trajectory, RecFM recursively models a family of trajectories spanning different inference-time traversal scales and enforces consistency among them. In particular, trajectories at different scales are coupled by aligning states that correspond to the same underlying point along the path, ensuring that predictions remain coherent across discretizations. This multi-scale coupling provides additional supervision and improves stability in one- or few-step regimes. Our main contributions include:

- **Recursive Flow Matching:** A novel flow matching framework for forecasting complex physical dynamics, enabling a unified treatment of systems governed either by explicit PDE formulations or by implicitly learned data-driven dynamics.
- **Multi-Scale Trajectory Alignment:** A mechanism that enforces consistency of trajectories across sampling scales, stabilizing dynamical rollouts and mitigating error accumulation over multiple inference steps.
- **High-Efficiency Emulation:** We validate our approach on both simulated and real-world physical dynamics prediction benchmarks, achieving state-of-the-art accuracy with substantially fewer sampling steps.

2. Background

In this section, we introduce the necessary background for our proposed *RecFM*. We briefly review generative and trajectory flow matchings, which form the core building blocks of our framework.

2.1. Flow Matching

Flow Matching (FM) (Lipman et al., 2022) is a simulation-free paradigm for training Continuous Normalizing Flows by regressing onto a target vector field. Let p_0 denote the target data distribution and p_1 denote a tractable source distribution (*e.g.*, a standard Gaussian). FM seeks to learn a time-dependent vector field $v_t(x;\theta) : \mathbb{R}^d \to \mathbb{R}^d; t \in [0,1]$ that defines a probability path p_t connecting p_0 and p_1. The transformation of a sample $x_0 \sim p_0$ to $x_1 \sim p_1$ is governed by the ordinary differential equation (ODE):

$$\frac{d\psi_t(x)}{dt} = v_t(\psi_t(x), t), \quad \psi_0(x) = x_0 \tag{1}$$

where ψ_t represents the flow map. To ensure tractability, Conditional Flow Matching (CFM) utilizes a per-sample regression objective:

$$\mathcal{L}_{\text{CFM}}(\theta) = \mathbb{E}_{t\sim U, x_0\sim p_0, x_1\sim p_1}[\|v_t(x_t,t;\theta) - u_t(x_t|x_0,x_1)\|^2] \tag{2}$$

where $u_t(x_t|x_0,x_1)$ is the conditional velocity field. A prevalent choice is the Optimal Transport (OT) path, which utilizes linear interpolation $x_t = (1-t)x_0 + tx_1$ to yield a constant target velocity $u_t(x_t|x_0,x_1) = x_1 - x_0$. Although this formulation fully specifies the generative process, its

practical performance is largely determined by the structure of the induced trajectories, motivating a closer examination of trajectory design.

The choice of trajectory (*i.e.*, the transport map) plays a key role in determining sampling efficiency and stability. Approaches focusing on Trajectories of Flow Matching (Zhang et al., 2024; Islam et al., 2025), to parameterize the drift and diffusion terms to model stochastic and irregularly sampled time series. From a physical perspective, such trajectories can be interpreted as approximations of the underlying system dynamics, where geometric simplicity contributes to stable and accurate generation. Yet existing methods fail to maintain consistency across discretization scales, compromising both accuracy and physical fidelity.

2.2. Self-Consistency and the Flow Map

To overcome the iterative bottleneck of FM, recent work has introduced the self-consistency property (Frans et al., 2024; Xu et al., 2023a). For a flow map $\mathbf{X}_{s,t} : \mathbb{R}^d \to \mathbb{R}^d$ that transports a state from time s to time t, self-consistency requires that all points along a single trajectory map to the same endpoint. This is formally described by the semigroup condition:

$$\mathbf{X}_{u,t}(\mathbf{X}_{s,u}(x)) = \mathbf{X}_{s,t}(x)$$

for all s, u, t such that $0 \leq s \leq u \leq t \leq 1$ where u is an intermediate timestep. In "one-step" models, a consistency function $f_\theta(x_t, t)$ is trained to satisfy $f_\theta(x_t, t) = x_1$ for all $t \in [0, 1]$. By executing this condition, the model ensures that the generated path remains unchanged, whether it is traversed in a single large step or in multiple smaller increments. This is an advanced regularization that can "straighten" the ODE trajectory and minimize the common truncation errors in accelerator solvers.

3. Recursive Flow Matching

We draw inspiration from the recursive movement of an ideal[1] wall-bouncing pendulum to design our method, *RecFM*. Below, we introduce the pendulum model, followed by the secondary trajectory formulation and the updated loss function for RecFM.

3.1. Physics Intuition

Let's consider the classical physics toy problem of a 1D wall-bouncing pendulum, illustrated in Figure 2. Let $x(t)$ and $v(t)$ be the position and velocity of the pendulum at time t respectively. Away from the wall at $x = 0$, the pendulum travels at **constant speed** governed by:

$$\dot{x}(t) = v(t), \quad \dot{v}(t) = 0$$

A bounce occurs every time the pendulum strikes the wall ($x = 0$), resulting in a set of trajectories. At each collision,

[1]We do not consider energy loss due to friction or drag forces.

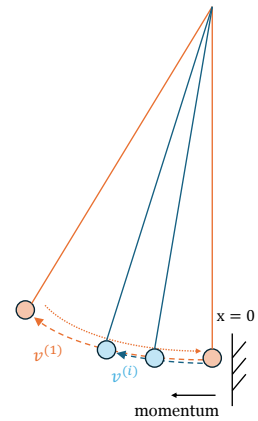

Figure 2. Pendulum trajectories and velocities for the primary trajectory ($v^{(1)}$, orange) and attenuated trajectories ($v^{(i)}$, $i > 1$, blue).

the velocity reverses direction and its magnitude is reduced, with a fraction $1 - \alpha^2$ of the kinetic energy lost, where $\alpha \in [0, 1]$ is the velocity retention coefficient. For simplicity, we consider velocities along a fixed direction (*e.g.*, from the wall toward the turning point), so that only their magnitudes are tracked across bounces. Let $v^{(i)}$ denote the velocity magnitude immediately after the i-th bounce. The collision update rule is:

$$v^{(i+1)} = \alpha\, v^{(i)}. \tag{3}$$

We assume a constant half-cycle duration across scales, consistent with small-angle dynamics, so that amplitude shrinks proportionally with velocity after each bounce. While not strictly physical, this yields a simple and tractable parameterization across trajectories.

After $D - 1$ collisions, we obtain a family of trajectories $\{v^{(i)}\}_{i=1}^{D}$ with progressively attenuated velocities. Writing $\boldsymbol{v}^* := v^{(1)}$ and $\alpha^{(i)} := \alpha^{i-1}$, we obtain the scaling relation

$$v^{(i)} = \alpha^{(i)}\, \boldsymbol{v}^*. \tag{4}$$

This velocity consistency defines a natural supervision signal for our multi-scale objective.

Figure 1 illustrates the key idea behind our approach. While vanilla flow matching learns a single trajectory between x_0 and x_1, we extend this formulation by introducing additional trajectories at different scales. Building on this intuition, we propose **Recursive Flow Matching** (*RecFM*), which enforces consistency across these trajectories.

3.2. RecFM Algorithm

Formulation. Given a data sample $x_0 \sim p_0$ and a noise sample $x_1 \sim p_1$, we define the standard linear interpolant

$$x_t = (1 - t)\, x_0 + t\, x_1, \qquad \boldsymbol{v}^* = x_1 - x_0. \tag{5}$$

Algorithm 1 Recursive Trajectory Training with Consistency Alignment

Require: Data distribution p_0, noise distribution p_1
Require: Velocity network $v_\theta(x, t, \alpha)$, recursion depth D
Require: Consistency weight λ, total training iterations N
  for iteration $n = 1$ to N **do**
    Sample $x_0 \sim p_0$ and $x_1 \sim p_1$
    Sample $t \sim \mathcal{U}(0, 1)$ and $\alpha \sim \mathcal{U}(t, 1)$
    $\boldsymbol{v}^* \leftarrow x_1 - x_0$
    $x_t \leftarrow (1-t)x_0 + tx_1$ {Shared spatial point}
    for $i = 1$ to D **do**
      $\alpha^{(i)} \leftarrow \alpha^{i-1}$ {Recursive trajectory scale}
      $\tau^{(i)} \leftarrow t/\alpha^{(i)}$ {Aligned trajectory time}
      $\hat{v}^{(i)} \leftarrow v_\theta(x_t, \tau^{(i)}, \alpha^{(i)})$ {Predicted velocity}
      $\mathcal{L}^{(i)}_{\text{traj}} \leftarrow \|\hat{v}^{(i)} - \alpha^{(i)}\boldsymbol{v}^*\|_2^2$
    end for
    for $i = 2$ to D **do**
      $\mathcal{L}^{(i)}_{\text{cons}} \leftarrow \|\hat{v}^{(i)} - \alpha^{(i)}\hat{v}^{(1)}\|_2^2$
    end for
    $\mathcal{L}_{\text{total}} \leftarrow \sum_{i=1}^{D} \mathcal{L}^{(i)}_{\text{traj}} + \lambda \sum_{i=2}^{D} \mathcal{L}^{(i)}_{\text{cons}}$
    Update θ using $\nabla_\theta \mathcal{L}_{\text{total}}$
  end for

The velocity network $v_\theta(x, t, \alpha)$ is conditioned on both time t and scale α, so that a single model represents the entire family of trajectories.

Consider a recursive formulation with depth D, where D trajectories are defined by time-scale pairs $\{(\tau^{(i)}, \alpha^{(i)})\}_{i=1}^{D}$. The rescaled time is defined as $\tau^{(i)} = t/\alpha^{(i)} \in [0, 1]$, with $\alpha^{(1)} = 1$ and $\tau^{(1)} = t$. Let $\hat{v}^{(i)} = v_\theta(x_t, \tau^{(i)}, \alpha^{(i)})$ denote the predicted velocity of the i-th trajectory. Under this alignment, all trajectories pass through the same spatial point x_t, yielding the cross-scale consistency relation

$$\hat{v}^{(i+1)} = \alpha\, \hat{v}^{(i)}. \tag{6}$$

This shared spatial point, which is visited by trajectories of different scales at correspondingly aligned times, is the structural property RecFM exploits.

Algorithm. We present Algorithm 1, which trains a velocity network on D recursive trajectories passing through the same point x_t: a primary trajectory (*i.e.*, $i = 1$) that learns the standard noise-to-data velocity $x_1 - x_0$, and $D - 1$ time-rescaled secondary trajectories parameterized by $\alpha^{(i)}$, whose target velocities are given by $\alpha^{(i)}(x_1 - x_0)$, inspired by the wall-bouncing dynamics in Section 3.

Training Objective. To enforce alignment across trajectory scales, we build on the recursive formulation above. The overall training objective aggregates supervision across all scales and enforces consistency with the primary trajectory:

$$\begin{aligned} \mathcal{L}_{\text{total}} &= \sum_{i=1}^{D} \mathcal{L}^{(i)}_{\text{traj}} + \lambda \sum_{i=2}^{D} \mathcal{L}^{(i)}_{\text{cons}} \\ \text{where } \mathcal{L}^{(i)}_{\text{traj}} &= \left\| \hat{v}^{(i)} - \alpha^{(i)} \boldsymbol{v}^* \right\|_2^2, \\ \mathcal{L}^{(i)}_{\text{cons}} &= \left\| \hat{v}^{(i)} - \alpha^{(i)} \hat{v}^{(1)} \right\|_2^2. \end{aligned} \tag{7}$$

Inference Sampling. Inference in RecFM is conducted by numerically solving the ODE defined by the learned velocity field $\hat{v}_\theta(x_t, t, \alpha)$. For single-step generation, using a first-order Euler step of size h, RecFM maps a noise sample $x_1 \sim p_1$ to the data manifold in one function evaluation:

$$x_0 \approx x_1 - h\, \hat{v}_\theta(x_1, 1, 1) \tag{8}$$

where $h = 1$, corresponding to integrating the trajectory over the full time horizon.

For multi-step generation, discretizing the trajectory into K steps $1 = t_0 > \cdots > t_K = 0$ with step sizes $h_k = t_{k-1} - t_k$, we iteratively update:

$$x_{t_k} = x_{t_{k-1}} - h_k\, \hat{v}_\theta(x_{t_{k-1}}, t_{k-1}, 1), \quad k = 1, \ldots, K. \tag{9}$$

By enforcing cross-scale velocity consistency during training, RecFM learns trajectories that remain stable under larger integration steps, enabling accurate few-step generation.

3.3. Theoretical results

We present Theorem 3.1 to show that adding recursive trajectories and cross-scale trajectory consistency loss accelerates the convergence of RecFM.

Theorem 3.1 (Truncation Error Reduction via Trajectory Straightening)**.** *Let $\hat{v}_\theta(x, t, \alpha)$ be the predicted velocity and $\mathbf{a}(x, t) = \partial_t\, v_\theta(x, t, 1) + (\nabla_x v_\theta)\, v_\theta(x, t, 1)$ denote the trajectory acceleration. The K-step Euler generation error with step size $h = 1/K$ satisfies*

$$\left\| \psi_1 - \hat{\psi}_1 \right\| \;\le\; \frac{h}{2} \frac{e^L - 1}{L} \sup_{t \in [0,1]} \|\mathbf{a}(\psi_t, t)\|, \tag{10}$$

where $L = \sup_t \|\nabla_x v_\theta(\cdot, t, 1)\|_{\text{op}}$. The acceleration decomposes into a temporal component and an advective term, $\mathbf{a} = \partial_t v_\theta + (\nabla_x v_\theta)\, v_\theta$. Minimizing $\mathcal{L}_{\text{cons}}$ enforces the cross-scale consistency condition

$$t\, \partial_t\, v_\theta(x, t, 1) \;+\; v_\theta(x, t, 1) \;=\; \partial_\alpha\, v_\theta(x, t, 1), \tag{11}$$

which constrains $\|\partial_t v_\theta\|$ and thereby reduces $\|\mathbf{a}\|$, tightening (10).

Proof. See Appendix B. □

Why does RecFM work?

A given interpolated state x_t lies on infinitely many trajectories indexed by α. Vanilla FM exploits only one of them, providing a single regression target $\boldsymbol{v}^*$ per sample. RecFM uses every (τ, α) pair as an independent supervisory signal for the *same* underlying directional quantity $x_1 - x_0$ at the *same* spatial point, while following the marginal distribution (Theorem B.2). This functions as data augmentation in the conditioning space of the network and is particularly valuable in the one-step regime, where generation quality depends entirely on a single evaluation $v_\theta(x_0, 0, 1)$. By coupling predictions across scales, RecFM enriches the gradient signal at every training point and removes the warm-up phase typically required by shortcut or consistency-style training (Appendix H).

4. Related Work

Neural PDE Solvers and Physics-Informed Learning. Early advancements in scientific machine learning focused on directly embedding physical laws into neural architectures to solve boundary value problems with minimal data. Physics-Informed Neural Networks (PINNs) (Raissi et al., 2019) penalize PDE residuals at randomly sampled collocation points, while neural operators like Fourier Neural Operators (Li et al., 2020) and DeepONet (Lu et al., 2021), Equivariant Neural fields (Knigge et al., 2024) use functional mappings between infinite-dimensional spaces. To address the limitation of the availability of high-fidelity data, multi-fidelity PINNs (Penwarden et al., 2022) were introduced to utilize low-fidelity responses as regularizers. However, these deterministic methods often struggle in complex settings and with real-world observations. By producing point estimates rather than predictive distributions, they offer limited uncertainty quantification and are rarely evaluated using probabilistic metrics, which can lead to physically inconsistent outputs.

Probabilistic Generative Modeling for Spatiotemporal Physics Systems. Probabilistic approaches quantify and calibrate uncertainty, providing a useful framework for learning physics-based systems. DiffusionPDE (Huang et al., 2024) and FunDPS (Yao et al., 2025) unify the forward and backward problems through joint coefficient-solution state modeling, while VideoPDE (Li et al., 2025) regards various tasks as video restoration to preserve fine-grained spectral details. A notable advancement is DYffusion (Rühling Cachay et al., 2023), which replaces standard Gaussian perturbations with a dynamics-informed temporal interpolation. By avoiding the high memory overhead of video-based models like MCVD (Voleti et al., 2022), DYffusion leverages Monte Carlo dropout to produce probabilistic ensembles during inference. In physics and climate science, foundation models (Aich et al., 2026; Ohana et al., 2024; Tauberschmidt et al., 2025) can achieve high accuracy with simple finetuning. Similarly, Rolling Sequence Diffusion Models (Ruhe et al., 2024; Wu et al., 2023) and ERDM (Cachay et al., 2025) utilize adaptive noise schedules to reflect the growth of uncertainty, prioritizing the ability to transition from deterministic to random horizons.

Accelerated Inference and Consistency-Based Models. Diffusion's iterative bottleneck has spurred recent studies on inference acceleration of generative models. EDM (Karras et al., 2022) provides efficient sampling that reduces sampling time for various tasks like molecular design (Vadgama et al., 2025). Rectified Flow (Liu et al., 2022) reduces transportation costs by training new ODEs on the previous flow generation pairs, optimizing the generation to a one-step path, while Shortcut Model (Frans et al., 2024) stabilizes sampling through interval self-consistency. Recent innovations like MeanFlow (Geng et al., 2025) have introduced average velocity fields to characterize transitions, while Drifting Diffusion (Deng et al., 2026) performs few-step generation in feature space. Generalized flow maps (Davis et al., 2025) show few-step generation on arbitrary Riemannian manifolds. Physics-informed methods like PBFM (Baldan et al., 2026) further apply these ideas to physical dynamics by incorporating explicit PDE residuals into the objective. However, such methods are fundamentally constrained by their reliance on known physical formulas, making them unsuitable for complex systems where equations are unavailable or computationally prohibitive to implement. RecFM addresses these concerns by introducing a recursive framework in the data space to enforce flow trajectory across discretization scales. By adopting this approach without explicitly using PDE residual supervision, RecFM provides a robust solution for high-fidelity emulation in complex scientific domains.

5. Experiments

5.1. Datasets

We evaluate our methods on three different dynamic physics datasets characterized by non-linear evolution and diverse spectral features. Specific technical configurations and simulation details are provided in Appendix A.

Sea Surface Temperatures (SST). This real-world climate dataset is adapted from the DYffusion benchmark (Rühling Cachay et al., 2023), using daily global measurement data from the NOAA OISSTv2 (Huang et al., 2021) product. Its spatial resolution is $1/4°$. We utilized a regional 60×60 latitude and longitude grid in the eastern tropical Pacific to simulate the long-term time-dependent relationship of the ocean temperature field.

Navier-Stokes Flow. We follow the experimental setup of DYffusion (Otness et al., 2021; Rühling Cachay et al., 2023) to evaluate fluid dynamics rollouts. The environment consists of an incompressible channel flow past four randomly

Table 1. Quantitative forecasting results for Sea Surface Temperature, Navier-Stokes Flow, and Helmholtz Staircase Equation. Lower values are better for MSE and CRPS, while the optimal SSR is 1. Best results in **bold**, second best underlined, third best in gray.

Method	SST				Navier-Stokes			Helmholtz Staircase		
	CRPS	MSE	SSR	Time [s]	CRPS	MSE	SSR	CRPS	MSE	SSR
Perturbation*	0.281	0.180	0.411	0.4241	0.090	0.028	0.448	0.218	0.111	0.004
Dropout*	0.267	0.164	0.406	0.4241	0.078	0.027	0.715	0.099	0.049	0.631
DDPM*	0.246	0.177	0.674	0.3054	0.180	0.105	0.573	0.156	0.153	0.563
MCVD*	0.216	0.161	0.926	79.167	0.154	0.070	0.524	0.137	0.128	0.867
DYffusion*	0.224	0.173	1.033	4.6722	0.067	0.022	0.877	0.144	0.106	1.121
VideoPDE (Li et al., 2025)	0.216	0.162	0.746	19.753	0.033	0.0068	0.205	0.026	5.6e-4	4.334
Vanilla FM	0.260	0.232	0.914	1.5202	0.036	0.0076	0.911	0.030	6.5e-4	1.485
RecFM (1-step)	0.217	0.162	0.984	0.4310	**0.031**	**0.0064**	**0.959**	0.0034	4.2e-5	**1.090**
RecFM (2-step)	**0.216**	**0.161**	**1.004**	0.7353	0.032	0.0068	0.932	**0.0027**	**2.7e-5**	1.440

*Results for SST and Navier-Stokes are reproduced from DYffusion (Rühling Cachay et al., 2023).

generated circular obstacles, inducing complex turbulence and vorticity patterns. The kinematic viscosity is set to $\nu = 10^{-3}$, and simulations are conducted on a 221×42 grid. The dataset comprises three channels: the velocity components in each spatial direction and the pressure field.

Helmholtz Staircase Equation. We follow the setup of The Well (Ohana et al., 2024). This benchmark corresponds to a higher-order analytical solution for acoustic scattering from a point source near an infinite, periodic "staircase" boundary. The simulated fields are discretized into 1024×256 grids to capture both the real and imaginary components of the pressure field. Accordingly, the dataset consists of two channels representing the real and imaginary parts.

5.2. Experiment Setup

5.2.1. Forecasting Configuration

We evaluate performance across varying temporal horizons:

Temporal Horizons and Autoregressive Rollout. For SST, we predict 7 days ahead from a 1-day input. For Navier-Stokes and Helmholtz, we respectively perform complete trajectory reconstructions of 64 and 49 steps starting from the initial state. To manage these long-range sequences, models are applied autoregressively: Navier-Stokes models predict 16 frames each time, while Helmholtz models generate 7 frames, unless specified.

Ensemble Generation. For all probabilistic metrics (CRPS, SSR), we create $M = 50$ ensemble members per initial condition to ensure statistical reliability.

Model Architecture and Efficiency. We apply RecFM to a pixel-level temporal DiT backbone, following the design introduced in (Li et al., 2025). All inference time measurements are performed on a single NVIDIA L40S GPU. RecFM is evaluated in both single- and multi-step regimes. More details of model architecture and implementation are included in Appendix D.

Hyperparameter Selection. We use $\lambda = 1$ for the consistency loss weight, with further analysis provided in Section 5.4. We adopt the depth-2 formulation for RecFM, corresponding to a primary trajectory with $\alpha^{(1)} = 1$ and a secondary trajectory with scale $\alpha^{(2)} = \alpha$, as it provides the best performance and efficiency (see Appendix C.2).

5.2.2. Baselines

We compare RecFM against a comprehensive suite of generative and stochastic benchmarks. For standard forecasting models, we adopt the experimental configuration and model suite from DYffusion (Rühling Cachay et al., 2023), which includes:

- **Stochastic Methods: Perturbation** and **Dropout** (Monte Carlo dropout at inference).
- **Iterative Models: DDPM** and **MCVD**, which utilize Gaussian noising processes.
- **Dynamics-Informed Solvers: DYffusion**, which directly couples diffusion steps with physical timesteps.

We further include benchmarks with state-of-the-art generative backbones:

- **VideoPDE (Li et al., 2025):** A unified solver that recasts PDE solving as hierarchical video inpainting using a pixel-space hierarchical transformer.
- **Vanilla FM:** Utilizes the identical architectural backbone to RecFM but is trained using a standard Flow Matching objective without the recursive feature.

We exclude PBFM (Baldan et al., 2026) from our primary comparisons as it requires explicit closed-form PDE residuals, which are impractical for complex, data-rich systems like global SST measurements. Comparison of PDE-governed data with physics-informed metrics is included in Appendix F. One-step methods such as MeanFlow (Geng et al., 2025) and Shortcut Models (Frans et al., 2024) and

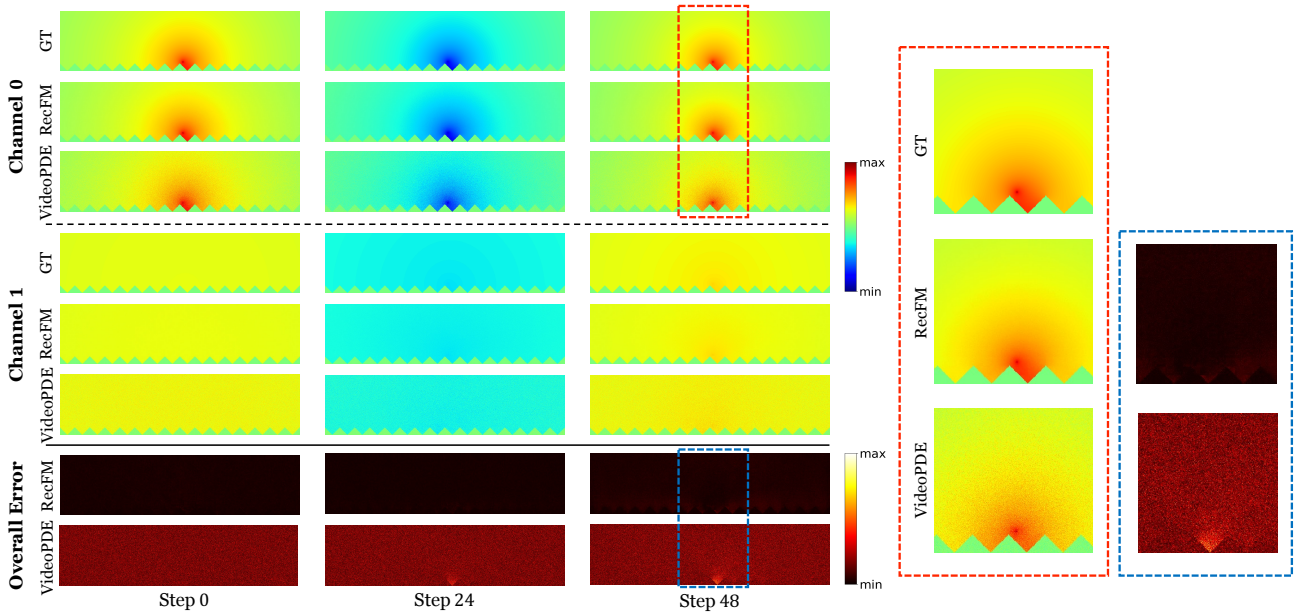

Figure 3. **Roll-out results of the Helmholtz Staircase equation.** Visual comparison of Ground Truth against RecFM and VideoPDE (best-performed baseline) for two channels, with the bottom rows indicating absolute errors. Columns correspond to dataset timesteps. The variation observed at Step 48 is displayed in an enlarged view on the right.

other benchmarks like Rectified Flow (Liu et al., 2022) are primarily designed for static generation and are therefore not included in our main comparisons. A comparison with Shortcut Models on Helmholtz Staircase is included in Appendix H.

5.2.3. Evaluation Metrics

To evaluate the fidelity and calibration of probability prediction, we employ three standard metrics:

Continuous Ranked Probability Score (CRPS) (Matheson & Winkler, 1976). A strictly proper scoring rule to measure the accuracy of the cumulative distribution function F relative to the observation y:

$$\mathrm{CRPS}(F, y) = \int_{-\infty}^{\infty} (F(z) - \mathbf{1}[z \geq y])^2 dz \tag{12}$$

In practice, we use the unbiased "fair" estimator for M ensembles.

Mean Squared Error (MSE). Measures the deterministic accuracy of the ensemble mean prediction $\bar{x}$ against the ground truth y for the dataset of size S:

$$\mathrm{MSE} = \frac{1}{S} \sum_{j=1}^{S} \|\bar{x}_j - y_j\|^2 \tag{13}$$

Spread-Skill Ratio (SSR). Evaluates the reliability of the ensemble by comparing the ensemble spread to the RMSE of the ensemble mean. An ideal ratio of 1.0 indicates a perfectly calibrated ensemble. Specifically, SSR values smaller than 1.0 indicate underdispersion, while values larger than 1.0 indicate overdispersion.

5.3. Forecasting Results

Quantitative results across all benchmarks are summarized in Table 1, with standard deviations in Appendix G. We evaluate RecFM using one- and two-step inference to highlight its flexibility, with additional analysis of step size in Appendix C.1. Overall, RecFM consistently achieves state-of-the-art performance in both fidelity and efficiency. In particular, it attains up to a 20× speedup over the diffusion-based baseline VideoPDE while also improving predictive accuracy and calibration. This speedup is measured in terms of total rollout runtime, reflecting the reduced number of inference steps required by RecFM. On the Helmholtz Staircase equation, RecFM achieves a 10× reduction in error compared to VideoPDE, which is the best-performed baseline. We further visualize roll-out snapshots for both channels of the Helmholtz equation, along with corresponding error maps, in Figure 3. RecFM produces predictions that closely match the ground truth, while VideoPDE struggles to capture the circular wave propagation patterns. Additional visualizations are provided in Appendix E.

Moreover, compared to vanilla flow-matching methods, which typically require ∼5 inference steps, RecFM produces high-quality results with only 1-2 steps, achieving over 15% lower MSE and substantially better SSR scores.

Table 2. Ablation study on the effect of λ for the Navier-Stokes equation using the 1-step model and 5-step model. Here $\lambda = 0$ results in vanilla FM. Best results in **bold**.

	1-step model			5-step model		
λ	**CRPS** (↓)	**MSE** (↓)	**SSR** (→ 1)	**CRPS** (↓)	**MSE** (↓)	**SSR** (→ 1)
0.0	0.035	0.0074	0.957	0.039	0.0093	0.843
0.5	0.034	0.0071	1.024	0.040	0.0099	**0.855**
1.0	**0.031**	**0.0064**	0.959	**0.037**	**0.0083**	0.836
10.0	0.038	0.0089	**0.988**	0.039	0.0089	0.784
1000000	0.238	0.268	1.147	0.234	0.261	1.161

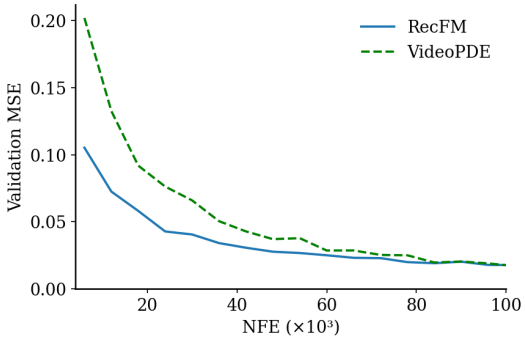

Figure 4. **Validation MSE versus NFE during training.** RecFM converges faster than the diffusion-based model VideoPDE and maintains consistently lower validation error.

We also observe that multi-step RecFM models do not consistently outperform single-step variants, as errors can accumulate over successive iterations.

While RecFM performs best across all tasks, its advantage is more pronounced on deterministic problems, such as PDE prediction tasks governed by explicit physical constraints, than on more stochastic data such as SST. This behavior is expected, as few-step flow matching is inherently more deterministic, which introduces minimal randomness into the sampling process.

Training Stability. We measure training progress of Navier-Stokes Flow in terms of the number of function evaluations (NFE), defined as the total number of vector field evaluations (*i.e.*, forward passes) during optimization. As shown in Figure 4, RecFM converges faster than the diffusion-based baseline (VideoPDE) and consistently achieves lower validation error throughout training.

5.4. Ablation Studies

We investigate the sensitivity of RecFM (see Equation 7) to the consistency loss weight λ on the Navier-Stokes equation. Table 2 reports results for both single-step and multi-step models over a wide range of λ values. A moderate setting (*e.g.*, $\lambda = 1.0$) consistently yields the best performance, suggesting that an appropriate balance between objectives is important. When λ is too small, the model places insufficient emphasis on trajectory consistency, which degrades performance. Interestingly, even without the self-consistency term ($\lambda = 0$), RecFM still surpasses the Vanilla FM baseline in Table 1, likely due to the presence of the secondary trajectory loss. In contrast, very large values (*e.g.*, $\lambda = 10^6$) cause the consistency term to overwhelm the primary flow-matching objective, leading to a marked drop in accuracy.

5.5. Image Generation Experiments

Although our primary focus is scientific emulation, RecFM also generalizes beyond physics-based systems, achieving competitive image quality with reduced training and inference cost (Appendix I).

6. Conclusion and Discussion

We introduced Recursive Flow Matching (RecFM), a framework that enforces consistency of generative trajectories across different sampling regimes. Our findings indicate that aligning trajectories across scales leads to an unexpected effect: using fewer inference steps can actually enhance both stability and accuracy, particularly in physics-based applications. This observation questions the usual trade-off between sampling efficiency and fidelity and suggests that the structure of the trajectory, rather than simply increasing the number of steps, is central to effective generation.

In experiments, RecFM delivers strong results on a range of scientific benchmarks, matching the performance of multi-step solvers while operating in the one- or few-step regimes and yielding notable speedups. These results highlight the potential of consistency-based approaches for real-time scientific emulation.

Limitations and Future Work. Despite these gains, extending RecFM to high-complexity real-world video remains challenging. Unlike physics-driven systems, natural videos involve rich semantic and temporal variations that may require modeling beyond standard flow matching trajectories. Although preliminary image-generation results are promising, scaling the framework to realistic video domains remains an open problem. Future work will further explore these settings and investigate RecFM as a general-purpose foundation model for multi-physics and real-world dynamical systems.

Impact Statement

RecFM enables efficient high-fidelity simulation, which can accelerate scientific research in areas such as climate modeling, fluid dynamics, and engineering design. By reducing computational cost, it supports real-time analysis and broadens access to advanced simulation tools. As with any data-driven approach, careful validation is important when deploying in real-world settings.

References

Abramson, J., Adler, J., Dunger, J., Evans, R., Green, T., Pritzel, A., Ronneberger, O., Willmore, L., Ballard, A. J., Bambrick, J., et al. Accurate structure prediction of biomolecular interactions with alphafold 3. *Nature*, 630 (8016):493–500, 2024.

Aich, M., Fürst, A., Sestak, F., Ruiz-Gonzalez, C., Boers, N., and Brandstetter, J. Wind: Weather inverse diffusion for zero-shot atmospheric modeling. *arXiv preprint arXiv:2602.03924*, 2026.

Baldan, G., Liu, Q., Guardone, A., and Thuerey, N. Physics vs distributions: Pareto optimal flow matching with physics constraints. In *The Fourteenth International Conference on Learning Representations*, 2026.

Benton, J., Deligiannidis, G., and Doucet, A. Error bounds for flow matching methods. *Transactions on Machine Learning Research*, 2024.

Cachay, S. R., Aittala, M., Kreis, K., Brenowitz, N., Vahdat, A., Mardani, M., and Yu, R. Elucidated rolling diffusion models for probabilistic forecasting of complex dynamics. *arXiv preprint arXiv:2506.20024*, 2025.

Cantwell, C. D., Moxey, D., Comerford, A., Bolis, A., Rocco, G., Mengaldo, G., De Grazia, D., Yakovlev, S., Lombard, J.-E., Ekelschot, D., et al. Nektar++: An open-source spectral/hp element framework. *Computer physics communications*, 192:205–219, 2015.

Chen, R. T. and Lipman, Y. Flow matching on general geometries. *arXiv preprint arXiv:2302.03660*, 2023.

Davis, O., Albergo, M. S., Boffi, N. M., Bronstein, M. M., and Bose, A. J. Generalised flow maps for few-step generative modelling on riemannian manifolds. *arXiv preprint arXiv:2510.21608*, 2025.

Deng, J., Dong, W., Socher, R., Li, L.-J., Li, K., and Fei-Fei, L. Imagenet: A large-scale hierarchical image database. In *2009 IEEE conference on computer vision and pattern recognition*, pp. 248–255. Ieee, 2009.

Deng, M., Li, H., Li, T., Du, Y., and He, K. Generative modeling via drifting. *arXiv preprint arXiv:2602.04770*, 2026.

Dhariwal, P. and Nichol, A. Diffusion models beat gans on image synthesis. *Advances in neural information processing systems*, 34:8780–8794, 2021.

Dhatt, G., Lefrançois, E., and Touzot, G. *Finite element method*. John Wiley & Sons, 2012.

Duncan, J. P., Wu, E., Dheeshjith, S., Subel, A., Arcomano, T., Clark, S. K., Henn, B., Kwa, A., McGibbon, J., Perkins, W. A., et al. Samudrace: Fast and accurate coupled climate modeling with 3d ocean and atmosphere emulators. *arXiv preprint arXiv:2509.12490*, 2025.

Frans, K., Hafner, D., Levine, S., and Abbeel, P. One step diffusion via shortcut models. *arXiv preprint arXiv:2410.12557*, 2024.

Geng, Z., Deng, M., Bai, X., Kolter, J. Z., and He, K. Mean flows for one-step generative modeling. *arXiv preprint arXiv:2505.13447*, 2025.

Ho, J., Jain, A., and Abbeel, P. Denoising diffusion probabilistic models. *Advances in neural information processing systems*, 33:6840–6851, 2020.

Huang, B., Liu, C., Banzon, V., Freeman, E., Graham, G., Hankins, B., Smith, T., and Zhang, H.-M. Improvements of the daily optimum interpolation sea surface temperature (doisst) version 2.1. *Journal of Climate*, 34(8): 2923–2939, 2021.

Huang, J., Yang, G., Wang, Z., and Park, J. J. Diffusionpde: Generative pde-solving under partial observation. *Advances in Neural Information Processing Systems*, 37: 130291–130323, 2024.

Islam, M. M., Kuipers, T. P., Vadgama, S., de Vente, C., Khan, A., Sánchez, C. I., and Bekkers, E. J. Longitudinal flow matching for trajectory modeling. *arXiv preprint arXiv:2510.03569*, 2025.

Karras, T., Aittala, M., Aila, T., and Laine, S. Elucidating the design space of diffusion-based generative models. *Advances in neural information processing systems*, 35: 26565–26577, 2022.

Knigge, D. M., Wessels, D. R., Valperga, R., Papa, S., Sonke, J.-J., Gavves, E., and Bekkers, E. J. Space-time continuous pde forecasting using equivariant neural fields. *Advances in Neural Information Processing Systems*, 37: 76553–76577, 2024.

Kovachki, N., Li, Z., Liu, B., Azizzadenesheli, K., Bhattacharya, K., Stuart, A., and Anandkumar, A. Neural operator: Learning maps between function spaces with applications to pdes. *Journal of Machine Learning Research*, 24(89):1–97, 2023.

Li, E., Wang, Z., Huang, J., and Park, J. J. Videopde: Unified generative pde solving via video inpainting diffusion models. *arXiv preprint arXiv:2506.13754*, 2025.

Li, Z., Kovachki, N., Azizzadenesheli, K., Liu, B., Bhattacharya, K., Stuart, A., and Anandkumar, A. Fourier neural operator for parametric partial differential equations. *arXiv preprint arXiv:2010.08895*, 2020.

Lipman, Y., Chen, R. T., Ben-Hamu, H., Nickel, M., and Le, M. Flow matching for generative modeling. *arXiv preprint arXiv:2210.02747*, 2022.

Liu, X., Gong, C., and Liu, Q. Flow straight and fast: Learning to generate and transfer data with rectified flow. *arXiv preprint arXiv:2209.03003*, 2022.

Lu, L., Jin, P., Pang, G., Zhang, Z., and Karniadakis, G. E. Learning nonlinear operators via deeponet based on the universal approximation theorem of operators. *Nature machine intelligence*, 3(3):218–229, 2021.

Ma, N., Goldstein, M., Albergo, M. S., Boffi, N. M., Vanden-Eijnden, E., and Xie, S. Sit: Exploring flow and diffusion-based generative models with scalable interpolant transformers. In *European Conference on Computer Vision*, pp. 23–40. Springer, 2024.

Matheson, J. E. and Winkler, R. L. Scoring rules for continuous probability distributions. *Management science*, 22 (10):1087–1096, 1976.

Mathieu, E. and Nickel, M. Riemannian continuous normalizing flows. *Advances in neural information processing systems*, 33:2503–2515, 2020.

Nichol, A. Q. and Dhariwal, P. Improved denoising diffusion probabilistic models. In *International conference on machine learning*, pp. 8162–8171. PMLR, 2021.

Ohana, R., McCabe, M., Meyer, L., Morel, R., Agocs, F. J., Beneitez, M., Berger, M., Burkhart, B., Dalziel, S. B., Fielding, D. B., et al. The well: a large-scale collection of diverse physics simulations for machine learning. *Advances in Neural Information Processing Systems*, 37: 44989–45037, 2024.

Otness, K., Gjoka, A., Bruna, J., Panozzo, D., Peherstorfer, B., Schneider, T., and Zorin, D. An extensible benchmark suite for learning to simulate physical systems. *arXiv preprint arXiv:2108.07799*, 2021.

Peebles, W. and Xie, S. Scalable diffusion models with transformers. In *Proceedings of the IEEE/CVF international conference on computer vision*, pp. 4195–4205, 2023.

Penwarden, M., Zhe, S., Narayan, A., and Kirby, R. M. Multifidelity modeling for physics-informed neural networks (pinns). *Journal of Computational Physics*, 451:110844, 2022.

Raissi, M., Perdikaris, P., and Karniadakis, G. E. Physics-informed neural networks: A deep learning framework for solving forward and inverse problems involving nonlinear partial differential equations. *Journal of Computational physics*, 378:686–707, 2019.

Rombach, R., Blattmann, A., Lorenz, D., Esser, P., and Ommer, B. High-resolution image synthesis with latent diffusion models. In *Proceedings of the IEEE/CVF conference on computer vision and pattern recognition*, pp. 10684–10695, 2022.

Ruhe, D., Heek, J., Salimans, T., and Hoogeboom, E. Rolling diffusion models. *arXiv preprint arXiv:2402.09470*, 2024.

Rühling Cachay, S., Zhao, B., Joren, H., and Yu, R. Dyffusion: A dynamics-informed diffusion model for spatiotemporal forecasting. *Advances in neural information processing systems*, 36:45259–45287, 2023.

Shen, Y., Wang, L., Yuan, H., Wang, Y., Yang, B., and Gu, Q. Simultaneous modeling of protein conformation and dynamics via autoregression. In *The Thirty-ninth Annual Conference on Neural Information Processing Systems*, 2025.

Song, J., Meng, C., and Ermon, S. Denoising diffusion implicit models. *arXiv preprint arXiv:2010.02502*, 2020.

Song, Y., Lorraine, J., Nie, W., Kreis, K., and Lucas, J. Multi-student diffusion distillation for better one-step generators. *arXiv preprint arXiv:2410.23274*, 2024.

Tauberschmidt, J., Fellenz, S., Vollmer, S. J., and Duncan, A. B. Physics-constrained fine-tuning of flow-matching models for generation and inverse problems. *arXiv preprint arXiv:2508.09156*, 2025.

Vadgama, S., Islam, M. M., Buracas, D., Shewmake, C., Moskalev, A., and Bekkers, E. Probing equivariance and symmetry breaking in convolutional networks. *arXiv preprint arXiv:2501.01999*, 2025.

Voleti, V., Jolicoeur-Martineau, A., and Pal, C. Mcvd-masked conditional video diffusion for prediction, generation, and interpolation. *Advances in neural information processing systems*, 35:23371–23385, 2022.

Watt-Meyer, O., Henn, B., McGibbon, J., Clark, S. K., Kwa, A., Perkins, W. A., Wu, E., Harris, L., and Bretherton, C. S. Ace2: accurately learning subseasonal to decadal atmospheric variability and forced responses. *npj Climate and Atmospheric Science*, 8(1):205, 2025.

Wu, T., Fan, Z., Liu, X., Zheng, H.-T., Gong, Y., Jiao, J., Li, J., Guo, J., Duan, N., Chen, W., et al. Ar-diffusion: Auto-regressive diffusion model for text generation. *Advances in Neural Information Processing Systems*, 36:39957–39974, 2023.

Xu, S., Huang, Y., Pan, J., Ma, Z., and Chai, J. Inversion-free image editing with natural language. *arXiv preprint arXiv:2312.04965*, 2023a.

Xu, S., Ma, Z., Huang, Y., Lee, H., and Chai, J. Cyclenet: Rethinking cycle consistency in text-guided diffusion for image manipulation. *Advances in Neural Information Processing Systems*, 36:10359–10384, 2023b.

Xu, Z.-Q. J., Zhang, L., and Cai, W. On understanding and overcoming spectral biases of deep neural network learning methods for solving pdes. *Journal of Computational Physics*, 530:113905, 2025.

Yao, J., Mammadov, A., Berner, J., Kerrigan, G., Ye, J. C., Azizzadenesheli, K., and Anandkumar, A. Guided diffusion sampling on function spaces with applications to pdes. *arXiv preprint arXiv:2505.17004*, 2025.

Zeni, C., Pinsler, R., Zügner, D., Fowler, A., Horton, M., Fu, X., Wang, Z., Shysheya, A., Crabbé, J., Ueda, S., et al. A generative model for inorganic materials design. *Nature*, 639(8055):624–632, 2025.

Zhang, X., Pu, Y., Kawamura, Y., Loza, A., Bengio, Y., Shung, D. L., and Tong, A. Trajectory flow matching with applications to clinical time series modelling. *Advances in Neural Information Processing Systems*, 37:107198–107224, 2024.

Zhuang, Y., Cheng, S., and Duraisamy, K. Spatially-aware diffusion models with cross-attention for global field reconstruction with sparse observations. *Computer Methods in Applied Mechanics and Engineering*, 435:117623, 2025.

A. Dataset Details

In this section, we provide the formal governing equations and technical implementation details for the physics datasets used in our evaluation. For every dataset that includes boundary conditions, these conditions are provided as extra constraints to each model.

A.1. Sea Surface Temperatures (SST)

The SST dataset is a real-world climate benchmark representing the daily evolution of sea surface temperature fields $\mathbf{T}$ over the eastern tropical Pacific Ocean. While not governed by a single closed-form PDE, the dynamics arise from complex ocean-atmosphere interactions and large-scale climate variability. Each sample consists of 11 spatial boxes, each represented as a 60×60 latitude-longitude grid with a single scalar channel corresponding to temperature values (Rühling Cachay et al., 2023). Following prior work, we use data from 1982 to 2019 for training, 2020 for validation, and 2021 for testing.

A.2. Navier-Stokes (NS) Flow

The Navier-Stokes benchmark simulates incompressible channel flow past random circular obstacles. The dynamics are governed by the following momentum and continuity equations:

$$\begin{aligned} \frac{\partial \mathbf{u}}{\partial t} + (\mathbf{u} \cdot \nabla)\mathbf{u} &= -\frac{1}{\rho}\nabla p + \nu \nabla^2 \mathbf{u} + \mathbf{f} \\ \nabla \cdot \mathbf{u} &= 0 \end{aligned} \tag{14}$$

where $\mathbf{u} = (u, v)$ is the velocity vector, p is the pressure field, ρ is the fluid density, and $\nu = 10^{-3}$ is the kinematic viscosity.

Technical Configuration:

- **Channels:** The dataset consists of 3 distinct channels: the x-velocity component (u), the y-velocity component (v), and the pressure field (p).
- **Preprocessing:** The raw simulation data is defined on a 221×42 grid. For the implementation of RecFM, Vanilla FM, and VideoPDE (Li et al., 2025), the input fields are bilinearly interpolated to a resolution of 220×40 before being passed to the model. During evaluation, the generated outputs are upsampled back to the original 221×42 resolution to compute metrics.

A.3. Helmholtz Staircase Equation

The Helmholtz benchmark evaluates acoustic scattering from a point source near a corrugated boundary. The steady-state pressure field u satisfies:

$$-(\Delta + \omega^2)u = \delta_{\mathbf{x}_0} \tag{15}$$

where Δ is the Laplacian, ω is the angular frequency, and $\mathbf{x}_0$ is the source position. The time-dependent pressure evolution is defined analytically as:

$$U(t, \mathbf{x}) = u(\mathbf{x})e^{-i\omega t} \tag{16}$$

Although the time dependence is analytically separable and purely periodic, such that the full trajectory is determined by the spatial field at a single time, the dataset remains physically meaningful as it encodes coherent wave propagation and phase dynamics. This setting therefore serves as a controlled benchmark for evaluating physical consistency (see Appendix F), complementing more dynamically complex systems.

Technical Configuration:

- **Channels:** To represent the complex-valued pressure fields, the model processes 2 primary channels: the real component $Re(U)$ and the imaginary component $Im(U)$ of the acoustic pressure. For all models, the constant domain masks provided in the dataset (Ohana et al., 2024) are used as a third input channel.

B. Additional Theorems and Corollaries

Proposition B.1 (Trajectory Convergence)**.** *Let θ^* be a global minimizer of $\mathcal{L}_{\text{total}}$ over a sufficiently expressive function class. Let $x_t = (1-t)\,x_0 + t\,x_1$ with $x_0 \sim p_0$, $x_1 \sim p_1$, and $v^* = x_1 - x_0$. Then the global minimizer of $\mathcal{L}_{\text{pri}}$ recovers the conditional expectation*

$$v_{\theta^*}(x, t, 1) \;=\; \mathbb{E}[\,x_1 - x_0 \mid x_t = x\,]\,, \tag{17}$$

and generates the correct marginal path p_t for all $t \in [0,1]$ (Lipman et al., 2022). Jointly, the global minimizer of $\mathcal{L}_{\text{sec}}$ satisfies, for every $\alpha \in (0,1]$ and $\tau = t/\alpha$,

$$v_{\theta^*}(x,\,\tau,\,\alpha) \;=\; \alpha\, v_{\theta^*}(x,\,t,\,1), \tag{18}$$

with $\mathcal{L}_{\text{cons}} = 0$ holding automatically at this optimum.

Proof. The loss $\mathcal{L}_{\text{pri}} = \mathbb{E}_{t,x_0,x_1}[\|v_\theta(x_t,t,1) - v^*\|^2]$ is a conditional regression whose unique L^2 minimizer is the conditional expectation (17). By the theory of Continuous Normalizing Flows (Lipman et al., 2022), the ODE $\frac{\mathrm{d}\psi_t}{\mathrm{d}t} = v_{\theta^*}(\psi_t, t, 1)$ with $\psi_0 \sim p_0$ generates the correct marginal p_t. The secondary loss $\mathcal{L}_{\text{sec}} = \|\hat{v}_{\text{sec}} - \alpha\, v^*\|^2$ is minimized at

$$v_{\theta^*}(x_t,\,\tau,\,\alpha) \;=\; \alpha\,\mathbb{E}[x_1 - x_0 \mid x_t = x] \;=\; \alpha\, v_{\theta^*}(x_t,\,t,\,1), \quad \tau = t/\alpha,$$

so that $\mathcal{L}_{\text{cons}} = \|\hat{v}_{\text{sec}} - \alpha\,\hat{v}_{\text{pri}}\|^2 = 0$ by construction. □

Theorem B.2 (Marginal Preservation of the Secondary Trajectory)**.** *Let v_{θ^*} be as in Proposition B.1, and assume that $v_{\theta^*}(\cdot, t, \alpha)$ is Lipschitz in x uniformly over t and α. For a fixed $\alpha \in (0,1]$, consider the secondary trajectory ODE:*

$$\frac{dx}{d\tau} = v_{\theta^*}(x,\,\tau,\,\alpha), \qquad x(0) \sim p_0. \tag{19}$$

Let $\{q_\tau^{(\alpha)}\}_{\tau\in[0,1]}$ denote the probability path induced by this ODE. Then for all $\tau \in [0,1]$, $q_\tau^{(\alpha)}$ coincides with the marginal distribution of $(1-\alpha\tau)\,x_0 + \alpha\tau\,x_1$, where $x_0 \sim p_0$ and $x_1 \sim p_1$. In particular,

$$q_0^{(\alpha)} = p_0, \qquad q_1^{(\alpha)} = p_\alpha, \tag{20}$$

where p_α is the marginal distribution of $(1-\alpha)\,x_0 + \alpha\,x_1$.

Proof. Define the candidate path $\tilde{x}_\tau := (1-\alpha\tau)\,x_0 + \alpha\tau\,x_1$. Differentiating: $\frac{\mathrm{d}\tilde{x}_\tau}{\mathrm{d}\tau} = \alpha\,(x_1 - x_0)$. Its marginal velocity field is

$$u_\tau^{(\alpha)}(x) := \mathbb{E}\left[\frac{\mathrm{d}\tilde{x}_\tau}{\mathrm{d}\tau} \;\middle|\; \tilde{x}_\tau = x\right] = \alpha\,\mathbb{E}[x_1 - x_0 \mid \tilde{x}_\tau = x]\,.$$

Since $\tilde{x}_\tau$ is the linear interpolant at fraction $\alpha\tau$, it has the same distribution as x_t with $t = \alpha\tau$. Substituting into (17) and comparing with (18):

$$u_\tau^{(\alpha)}(x) = \alpha\, v_{\theta^*}(x, \alpha\tau, 1) = v_{\theta^*}(x, \tau, \alpha).$$

By uniqueness of solutions to the continuity equation under the Lipschitz assumption, the induced path $q_\tau^{(\alpha)}$ coincides with the marginal of $\tilde{x}_\tau$. Setting $\tau = 0$ and $\tau = 1$ gives (20). □

Proof of Theorem 3.1

Proof. **Part (i).** The bound (10) follows from the discrete Grönwall inequality applied to the Euler discretization error, as used in the flow matching error analysis of Benton et al. (Benton et al., 2024). The local truncation error of a single step of size h from ψ_s is $\frac{h^2}{2}\|\mathbf{a}(\psi_s, s)\| + O(h^3)$, and the global error accumulates via the Lipschitz constant L.

Part (ii). Set $\alpha = 1 - \epsilon$ for small $\epsilon > 0$. Then $\tau = t/(1-\epsilon) = t + t\epsilon + O(\epsilon^2)$. Taylor-expanding the consistency residual:

$$v_\theta(x_t, \tau, \alpha) - \alpha\, v_\theta(x_t, t, 1) \;=\; \epsilon[\,t\,\partial_t v_\theta(x_t, t, 1) + v_\theta(x_t, t, 1) - \partial_\alpha v_\theta(x_t, t, 1)\,] + O(\epsilon^2).$$

Therefore $\mathcal{L}_{\text{cons}}$ penalizes, at leading order, $\|t\,\partial_t v_\theta + v_\theta - \partial_\alpha v_\theta\|^2$. Setting this to zero yields the cross-scale coherence condition, which constrains $\|\partial_t v_\theta\|$ for bounded $\|\partial_\alpha v_\theta\|$ and $\|v_\theta\|$. Since $\partial_t v_\theta$ is one of the two components of the acceleration, reducing it tightens the global error bound (10). Vanilla FM trains only with $\mathcal{L}_{\text{pri}}$, which regresses v_θ onto v^* pointwise at each t without coupling different times, and therefore imposes no constraint on $\partial_t v_\theta$. □

Corollary B.3 (Consistent Few-Step Sampling)**.** *Let v_{θ^*} be as in Proposition B.1.*

(i) *For any $\alpha \in (0, 1]$, a single Euler step of size α along the* primary *trajectory at $t = 0$ yields a sample whose distribution matches the endpoint of the secondary trajectory:*

$$x_0 + \alpha\, v_{\theta^*}(x_0, 0, 1) \;\overset{d}{=}\; x_0 + \int_0^1 v_{\theta^*}\big(x(\tau), \tau, \alpha\big)\, d\tau \;\sim\; p_\alpha. \tag{21}$$

Consequently, the family of secondary trajectories indexed by α provides a continuum of self-consistent few-step samplers, each producing a valid interpolant marginal p_α regardless of the discretization granularity.

(ii) *By Theorem 3.1, one-step generation is exact if and only if the trajectory acceleration $\mathbf{a} \equiv 0$. Since $\mathcal{L}_{\text{cons}}$ directly penalizes $\|\partial_t v_\theta\|$, a component of $\|\mathbf{a}\|$, RecFM actively drives the trajectory toward the zero-curvature regime where few-step Euler integration is accurate. Vanilla FM imposes no such constraint, leaving trajectory curvature uncontrolled.*

C. Additional Results

C.1. Influence of Inference Steps

We further analyze the effect of the number of inference steps in RecFM. Figure 5 shows the MSE as a function of the number of inference steps on the Navier-Stokes task. RecFM achieves its best performance with one- or two-step generation. We hypothesize that this behavior is due to the largely deterministic nature of physics-governed systems, where longer sampling trajectories can introduce accumulated errors.

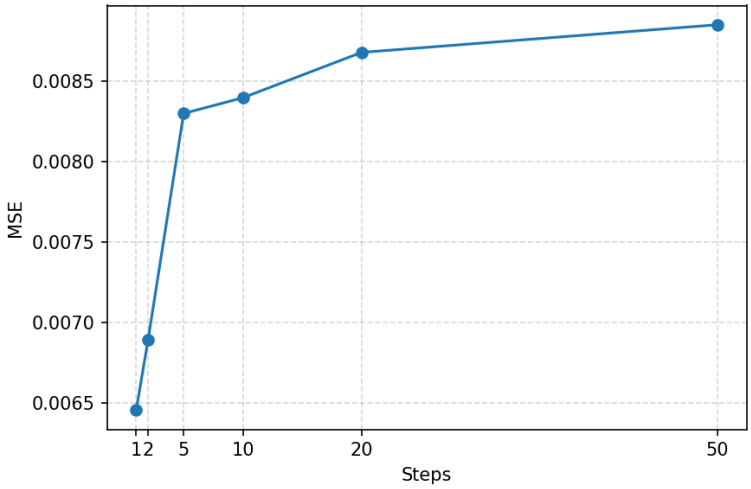

Figure 5. **MSE vs. inference steps on the Navier-Stokes benchmark.** RecFM achieves optimal performance with one- and two-step generation, while increasing the number of steps leads to error accumulation.

C.2. Influence of Recursion Depth D

We study the effect of recursion depth D on model performance. The depth D controls the number of trajectory scales used during training, thereby governing the strength of multi-scale supervision. While RecFM particularly corresponds to the depth-2 case in our main experiments, higher depths introduce additional consistency constraints across more trajectory scales.

Table 3 presents a comparison of different recursion depths on the Navier-Stokes benchmark. The vanilla FM ($D = 1$) needs multi-step inference (5 steps) to reach acceptable performance, whereas RecFM ($D = 2$) already achieves strong results with a single inference step. Raising the recursion depth to $D = 3$ leads to slightly inferior performance compared to $D = 2$, with small declines in MSE, SSR, and inference speed. In addition, training the depth-3 model requires larger memory than training the depth-2 RecFM due to the extra gradient terms introduced at depth 3. These observations indicate that enforcing

pairwise consistency is sufficient to obtain the advantages of multi-scale alignment, and that further increasing the recursion depth yields diminishing returns.

Based on these results, we adopt $D = 2$ as the default configuration in the main experiments, as it achieves strong performance while maintaining a simple and efficient formulation.

Table 3. Ablation study on recursion depth D for Navier-Stokes flow. Vanilla FM uses 5-step inference, while RecFM variants operate in the 1-step regime.

Depth D	**CRPS** (↓)	**MSE** (↓)	**SSR** (→ 1)	**Time [s]**
$D = 1$ (Vanilla FM, 5-step)	0.036	0.0076	0.911	6.914
$D = 2$ (RecFM, 1-step)	0.031	0.0064	0.959	1.588
$D = 3$ (extended RecFM, 1-step)	0.031	0.0065	1.091	1.594

C.3. Additional Training Dynamics and Convergence

We further compare validation MSE versus NFE during training for flow matching methods. Figure 6 shows that RecFM converges faster than Vanilla FM and maintains lower validation error, demonstrating improved efficiency and stability.

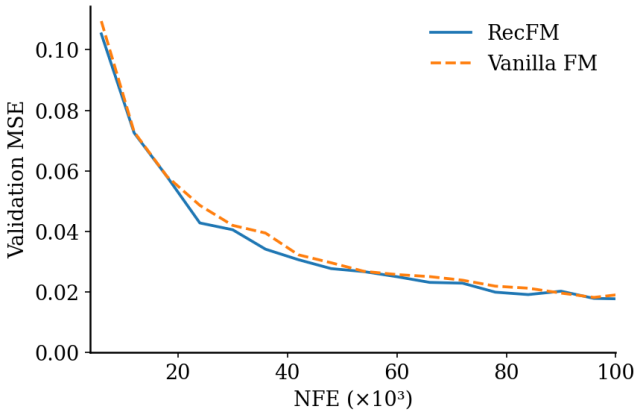

Figure 6. **Flow matching validation MSE versus NFE during training.** RecFM converges faster than Vanilla FM and maintains consistently lower validation error.

D. Architecture and Implementation Details

We adopt the state-of-the-art Hierarchical Video Diffusion Transformer (HV-DiT) backbone from VideoPDE (Li et al., 2025), with the sole modification that the input mask channel is removed. Unlike DYffusion (Rühling Cachay et al., 2023), whose forecasting-oriented formulation is not naturally compatible with transformer-based diffusion backbones such as HV-DiT, RecFM operates directly on the learned velocity field and can be integrated into existing spatiotemporal diffusion architectures with minimal modification. This also makes direct comparison against the original DYffusion architecture a more appropriate and fair evaluation setting.

During training, our recursive formulation requires D forward/backward gradient evaluations per iteration due to multi-scale trajectory supervision. To maintain comparable overall training cost, we reduce the total number of training iterations by the same factor D relative to other models.

A detailed overview of the model architecture and its hyperparameters (*e.g.*, for the Navier-Stokes equation with $D = 2$) is provided in Table 4.

Table 4. **RecFM training and model hyperparameters of Navier-Stokes Flow.**

Hyperparameter	RecFM (NS Flow)
Parameters	116.2M
Training steps	40k
Batch size	64
GPUs	4 × L40S
Mixed Precision	bfloat16
Patch Size ($T \times H \times W$)	[2, 2, 1]
Neighborhood Attention Levels	1
Global Attention Level	1
Neighborhood Attention Depth	2
Global Attention Depth	11
Feature Dimensions	[384, 768]
Attention Head Dimension	64
Neighborhood Kernel Size ($T \times H \times W$)	[2, 7, 7]
Mapping Depth	1
Mapping Width	768
Dropout	0
Optimizer	AdamW
Learning Rate	5×10^{-4}
$[\beta_1, \beta_2]$	$[0.9, 0.95]$
λ	1
Epsilon	1×10^{-8}
Weight Decay	1×10^{-2}

E. Additional Visualizations

Visualization of more timesteps of the Helmholtz Staircase equation is shown in Figure 7. Additionally, we visualize a representative Navier-Stokes rollout in Figure 8.

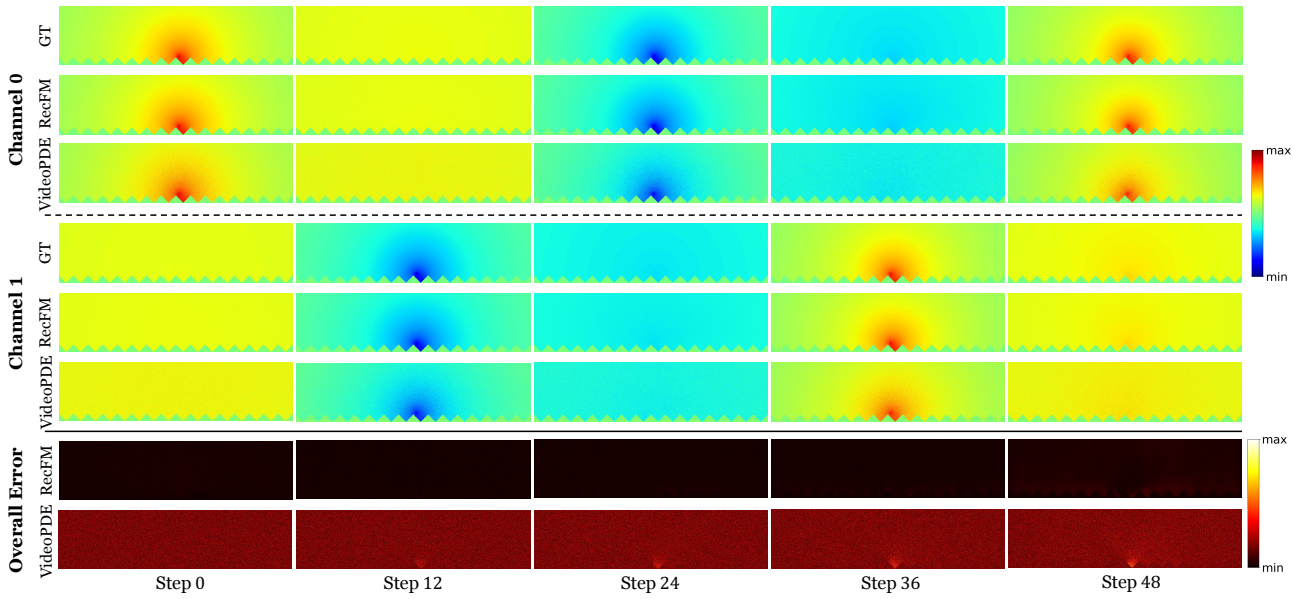

Figure 7. **More roll-out results of the Helmholtz Staircase equation.** Visual comparison of Ground Truth against RecFM and VideoPDE (best-performed baseline) for two channels, with the bottom rows indicating absolute errors. Columns correspond to dataset timesteps.

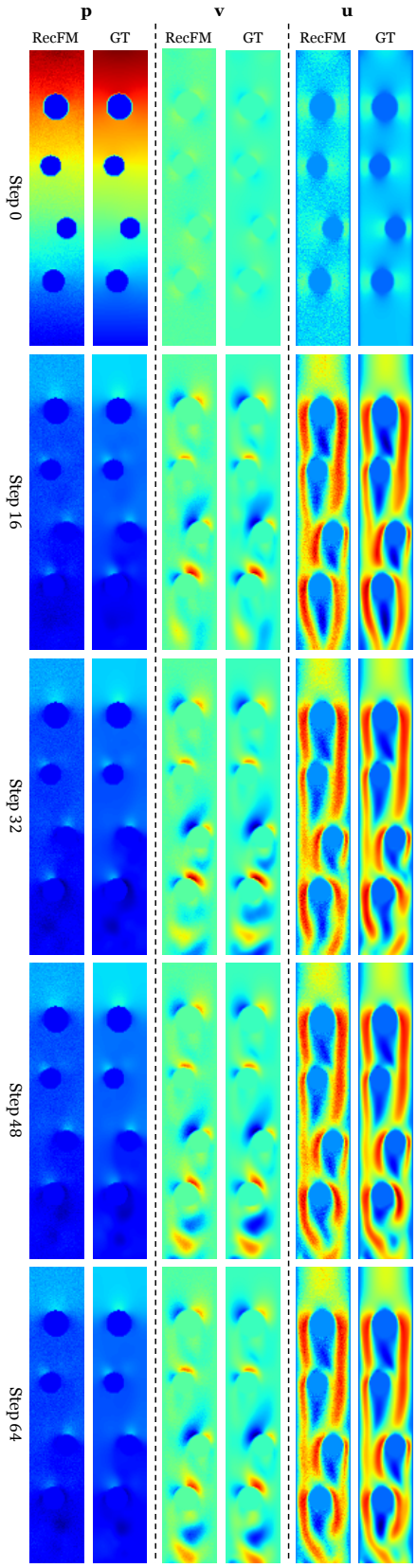

Figure 8. **Navier-Stokes rollout sample.**

F. Physics-Informed Evaluation

We further compare RecFM with PBFM (Baldan et al., 2026) on PDE-governed datasets in Table 5, following the original setting of 20 inference steps. While PBFM consistently improves over vanilla Flow Matching, its iterative refinement procedure limits both efficiency and accuracy relative to RecFM. In contrast, RecFM achieves higher accuracy while requiring only 1-2 inference steps, resulting in substantially faster generation.

To assess physical consistency, we additionally report physics-informed evaluation metrics. For the Navier-Stokes dataset, the trajectories are transient and do not reach a statistically stationary regime, making standard long-time turbulence diagnostics inapplicable. Instead, we evaluate the average kinetic energy $\langle E(t) \rangle$, normalized by the initial ground-truth energy $\langle E_{\text{real}}^{t=0} \rangle$. In Table 5, we report KE Accuracy, which measures the relative agreement between predicted and ground-truth energy (values closer to 1 indicate better physical fidelity). The rollout of kinetic energy is shown in Figure 9. While PBFM enforces strong physical constraints at each autoregressive iteration, errors accumulate over time. In contrast, RecFM maintains stable dynamics and achieves lower overall error without noticeable accumulation.

For the Helmholtz Staircase equation, we further report the PDE residual of the wave equation $\partial^2 U/\partial t^2 + \omega^2 U = 0$ in the table, where values closer to zero indicate better adherence to the governing dynamics.

These results demonstrate that RecFM not only produces visually accurate predictions, but also more faithfully preserves the underlying physical dynamics due to its few-step nature.

Table 5. Physics-informed quantitative forecasting results for Navier-Stokes Flow, and Helmholtz Staircase Equation. Lower values are better for MSE, CRPS, and PDE Residual, while SSR and KE Accuracy are optimal when closer to 1. Best results in **bold**.

Method	Navier-Stokes					Helmholtz Staircase			
	CRPS	MSE	SSR	KE Accuracy	Time [s]	CRPS	MSE	SSR	PDE Residual
VideoPDE (Li et al., 2025)	0.033	0.0068	0.205	0.9670	72.64	0.026	5.6e-4	4.334	0.00841
Vanilla FM	0.036	0.0076	0.911	0.9522	6.914	0.030	6.5e-4	1.485	0.01102
PBFM (Baldan et al., 2026)	0.034	0.0071	0.810	0.9592	14.75	0.0094	1.2e-4	0.737	0.00519
RecFM (1-step)	**0.031**	**0.0064**	**0.959**	**0.9791**	1.588	0.0034	4.2e-5	**1.090**	0.00476
RecFM (2-step)	0.032	0.0068	0.932	0.9672	3.128	**0.0027**	**2.7e-5**	1.440	**0.00457**

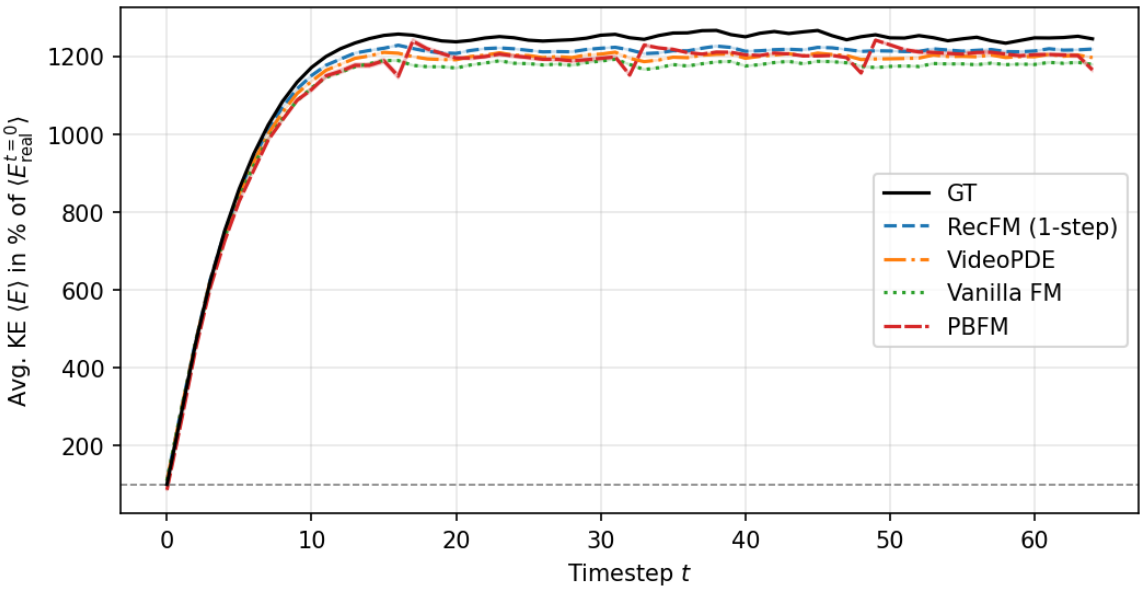

Figure 9. **Average kinetic energy over time.** $\langle E(t) \rangle$ normalized by $\langle E_{\text{real}}^{t=0} \rangle$. 100% corresponds to the initial ground-truth energy.

G. Statistical Significance

We additionally report the standard deviation of all metrics (CRPS, MSE, and SSR) for RecFM, VideoPDE, and Vanilla FM (*i.e.*, all methods using the HV-DiT backbone, as shown in Tables 6 and 7.

Table 6. Quantitative forecasting results (mean ± std) on SST and Navier–Stokes datasets. Lower CRPS and MSE are better, while SSR closer to 1 indicates better calibration.

Method	**SST**			**Navier–Stokes**		
	CRPS ↓	MSE ↓	SSR → 1	CRPS ↓	MSE ↓	SSR → 1
VideoPDE (Li et al., 2025)	$0.216_{\pm 0.005}$	$0.162_{\pm 0.002}$	$0.746_{\pm 0.007}$	$0.033_{\pm 0.002}$	$0.0068_{\pm 0.0003}$	$0.205_{\pm 0.013}$
Vanilla FM	$0.260_{\pm 0.007}$	$0.232_{\pm 0.002}$	$0.914_{\pm 0.006}$	$0.036_{\pm 0.001}$	$0.0076_{\pm 0.0001}$	$0.911_{\pm 0.008}$
RecFM (1-step)	$0.217_{\pm 0.003}$	$0.162_{\pm 0.001}$	$0.984_{\pm 0.006}$	$0.031_{\pm 0.001}$	$0.0064_{\pm 0.0001}$	$0.959_{\pm 0.003}$
RecFM (2-step)	$0.216_{\pm 0.003}$	$0.161_{\pm 0.001}$	$1.004_{\pm 0.007}$	$0.032_{\pm 0.001}$	$0.0068_{\pm 0.0001}$	$0.932_{\pm 0.004}$

Table 7. Quantitative forecasting results (mean ± std) on the Helmholtz Staircase dataset. Lower CRPS and MSE are better, while SSR closer to 1 indicates better calibration.

Method	CRPS ↓	MSE ↓	SSR → 1
VideoPDE (Li et al., 2025)	$0.026_{\pm 0.001}$	5.6e-4$_{\pm 1\text{e-}5}$	$4.334_{\pm 0.071}$
Vanilla FM	$0.030_{\pm 0.001}$	6.5e-4$_{\pm 1\text{e-}5}$	$1.485_{\pm 0.012}$
RecFM (1-step)	$0.0034_{\pm 0.0001}$	4.2e-5$_{\pm 1\text{e-}6}$	$1.090_{\pm 0.010}$
RecFM (2-step)	$0.0027_{\pm 0.0001}$	2.7e-5$_{\pm 1\text{e-}6}$	$1.440_{\pm 0.012}$

H. Shortcut Models vs. RecFM

Although both Shortcut Models (Frans et al., 2024) and RecFM enforce self-consistency to enable few-step generation, they impose structurally distinct constraints on the learned velocity field. Shortcut Models parameterize the network by a step-size d and enforce a *compositional* consistency condition: a single step of size $2d$ must produce the same result as two consecutive steps of size d,

$$x_t + 2d \cdot v_\theta(x_t, t, 2d) = \big(x_t + d \cdot v_\theta(x_t, t, d)\big) + d \cdot v_\theta\big(x_t + d \cdot v_\theta(x_t, t, d),\ t + d,\ d\big). \tag{22}$$

Crucially, the right-hand side evaluates v_θ at the *step-forward* state $x_t + d \cdot v_\theta(x_t, t, d)$, coupling the constraint to the spatial geometry of the trajectory. In contrast, RecFM conditions the network on a continuous scale parameter α and enforces a *pointwise scaling* relation at the same spatial location x_t:

$$\mathcal{L}_{\text{cons}} = \big\| v_\theta(x_t,\, \tau,\, \alpha) - \alpha\, v_\theta(x_t,\, t,\, 1) \big\|_2^2, \qquad \tau = t/\alpha. \tag{23}$$

No choice of the hyperparameters (α, λ) can reduce Equation 23 to Equation 22, because the former is evaluated at a single point while the latter intrinsically depends on a forward Euler update.

Despite this structural gap, the two constraints become locally equivalent in an infinitesimal limit. Setting $\alpha = 1 - \epsilon$ in the RecFM constraint and noting that $\tau = t/(1-\epsilon) \approx t + t\epsilon$, a first-order Taylor expansion of the left-hand side of Equation 23 around $(t, 1)$ gives $v_\theta(x_t, t, 1) + t\epsilon\, \partial_t v_\theta - \epsilon\, \partial_\alpha v_\theta$, while the right-hand side becomes $(1-\epsilon)\, v_\theta(x_t, t, 1)$. Equating and dividing by ϵ yields the leading-order constraint

$$t\, \partial_t v_\theta(x_t, t, 1) - \partial_\alpha v_\theta(x_t, t, 1) + v_\theta(x_t, t, 1) = 0, \tag{24}$$

which constrains how the velocity field varies with time and scale. The analogous expansion of the Shortcut condition 22 as $d \to 0^+$ instead produces a constraint involving the spatial Jacobian $\nabla_x v_\theta \cdot v_\theta$, because the forward evaluation point requires a spatial Taylor expansion. Both conditions penalize trajectory curvature at first order, but through complementary mechanisms: Shortcut Models regularize via spatial composition, while RecFM regularizes via cross-scale coherence. At the global optimum of either objective the velocity field recovers the constant OT velocity $v_\theta(x_t, t) = x_1 - x_0$, for which straight-line trajectories trivially satisfy both Equation 22 and Equation 23.

Intuition for the scaled velocity. The scaled velocity is never used at inference: generation always proceeds with $\alpha = 1$. Its role is purely as a *training scaffold*. A given interpolated state $x_t = (1-t)x_0 + tx_1$ lies simultaneously on a family of trajectories: the primary trajectory (from x_0 to x_1, at time t) and a secondary trajectory (from x_0 to the partial target $x_\alpha = (1-\alpha)x_0 + \alpha x_1$, at rescaled time $\tau = t/\alpha$). While the velocity scales trivially by α, the underlying directional estimation problem, recovering $x_1 - x_0$ from the noisy state x_t is shared across all scales. Each (τ, α) pair therefore provides an independent supervisory signal for the same directional quantity at the same spatial point, functioning as data augmentation in the conditioning space of the network. This is particularly beneficial in the one-step regime, where the entire generation quality depends on a single evaluation of $v_\theta(x_0, 0, 1)$: RecFM enriches the gradient information at every training point through the secondary and consistency losses, whereas vanilla flow matching provides only a single regression target per sample. Moreover, the flexibility of RecFM in selecting α removes the need for the warm-up phase often required in flow matching and diffusion-based shortcut models, leading to more stable and efficient training.

Performance Comparison on Physics Dynamics. In Table 8, we compare the Shortcut Model with RecFM on the Helmholtz Staircase dataset for 1-step generation. RecFM achieves better performance, while the Shortcut Model underperforms despite hyperparameters being carefully tuned to the best of our knowledge. We note that the Shortcut Model is primarily designed for static image generation, and extending it to dynamic settings presents additional challenges.

Table 8. 1-Step quantitative forecasting results for Helmholtz Staircase Equation.

Method	**Helmholtz Staircase**		
	CRPS	**MSE**	**SSR**
Shortcut Model (Frans et al., 2024)	0.0144	1.6e-4	0.467
RecFM	0.0034	4.2e-5	1.090

Figure 10. **Selected samples from our** 256×256 **resolution RecFM-XL model.**

I. Recursive Flow Matching for Image Generation

Table 9 presents the image generation performance of our proposed RecFM-XL model compared to other generative baselines. We report the Fréchet Inception Distance (FID) and evaluate all models with classifier-free guidance (CFG = 1.5) on the ImageNet-1k dataset (Deng et al., 2009). RecFM achieves an FID < 3 within 16 sampling steps. Our results show that RecFM is competitive in image generation as a multi-step flow matching method, while requiring fewer training epochs and inference steps compared with DiT (Peebles & Xie, 2023) and SiT (Ma et al., 2024). Notably, RecFM performs better with 16 inference steps than with 128, which we attribute to its training objective that emphasizes few-step generation, limiting improvements from additional steps.

Table 9. Comparison of generative models under different sampling regimes.

Model	FID ↓	Sampling Steps	Param Count	Epochs Trained
DiT-XL (Peebles & Xie, 2023)	2.27	500	675M	640
SiT-XL (Ma et al., 2024)	2.06	250	675M	640
ADM-G (Dhariwal & Nichol, 2021)	4.59	250	–	426
LDM-4-G (Rombach et al., 2022)	3.6	500	400M	106
Shortcut Model (XL) (Frans et al., 2024)	3.8	128	676M	250
RecFM-XL	2.53	128	675M	160
RecFM-XL	2.49	16	675M	160
RecFM-XL	3.22	8	675M	160

We further include some visualizations of RecFM-XL model with CFG, as shown in Figures 10, 11, 12.

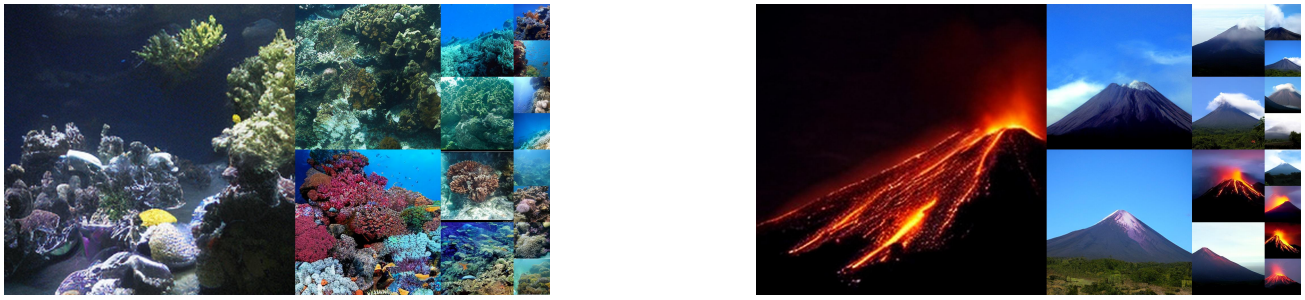

(a) Coral reef (973) *(b)* Volcano (980)

Figure 11. **Uncurated** 256×256 **RecFM-XL samples.** Each panel shows samples from a different ImageNet class.

(a) Macaw (88)

(b) Sulphur-crested cockatoo (89)

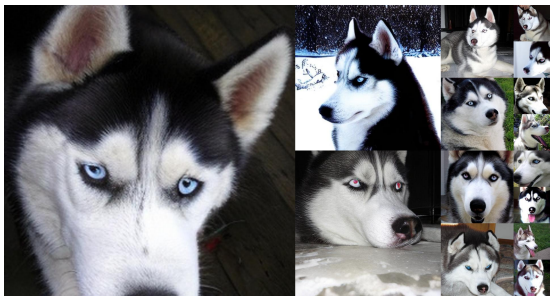

(c) Husky (250)

(d) Arctic wolf (270)

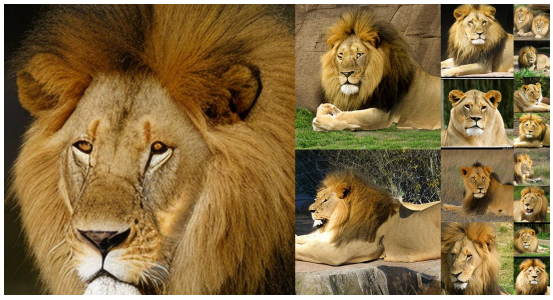

(e) Lion (291)

(f) Otter (360)

(g) Red panda (387)

(h) Panda (388)

(i) Balloon (417)

(j) Cliff drop-off (972)

Figure 12. **Uncurated** 256×256 **RecFM-XL samples (Continued).** Each panel shows samples from a different ImageNet class.